Inverse design of multistable kirigami metamaterial via geometry-enabled shape programming and transforming

Yanqi Yin,[1] Yunzhou Hu,[1] Yang Yu,[1] Yupei Zhang,[2,3] Chen Liu,[4] Wenjie Sun,[5,†] and Bo Li[1,*]

[1] *Shaanxi Key Laboratory of Intelligent Robots, School of Mechanical Engineering, Xi'an Jiaotong University, Xi'an, Shaanxi, 710049, People's Republic of China*

[2] *School of Future Technology, Xi'an Jiaotong University, Xi'an, Shaanxi, 710049, People's Republic of China*

[3] *Med-X Institute, The First Affiliated Hospital of Xi'an Jiaotong University, Xi'an, Shaanxi, 710061, People's Republic of China*

[4] *Wellcome/EPSRC Centre for Interventional and Surgical Sciences, University College London, WC1E 6BT London, United Kingdom*

[5] *School of Mechanical and Precision Instrument Engineering, Xi'an University of Technology, Xi'an, Shaanxi, 710048, People's Republic of China*

(Received 30 December 2024; revised 28 February 2025; accepted 4 March 2025; published 25 March 2025; corrected 4 April 2025)

The inverse design of metamaterials with desired properties represents a significant challenge in mechanical science. Despite the potential demonstrated by recent algorithm models, their adoption has been limited by constraints such as the geometric limitations of elementary building cells. The use of the kirigami principle, which offers large deformation and nonlinear stiffness, has been explored. However, existing kirigami geometries, which remain isotropic, may restrict the design space. Our objective is to leverage the capabilities of geometry in shape programming and transformation to provide a framework for inverse design. This framework utilizes a unified geometry in kirigami cutting that is easily parameterized to generate independent anisotropic deformation and bistability. By integrating machine learning with a genetic algorithm, we achieve an inverse design process. The resulting kirigami architectures can be preprogrammed into target shapes and transformed between multiple stable states. This work underscores the significance of cell geometry topology, offering a powerful tool for the inverse design of metamaterials with reconfigurable and tailored mechanical properties, applicable in various fields such as robotics, electronics, and beyond.

DOI: 10.1103/PhysRevApplied.23.034070

I. INTRODUCTION

Advancements in data-driven methods and optimization algorithms have significantly facilitated the development of metamaterials, providing a design paradigm in inverse programming [1–3]. In the realm of mechanical metamaterials, inverse design has garnered considerable attention [4–6], tailoring extraordinary mechanical characteristics [7–10]. By utilizing machine learning and genetic algorithms, researchers can design metamaterials without needing a comprehensive understanding of the complex relationship between structure and response [11]. Consequently, novel metamaterials can be designed inversely, paving the way for innovative applications and discoveries in the field such as sensing [12–14], flexible electronics [15,16], and energy absorption [17–19]. The foundation for functional implementation in programmable mechanical metamaterials significantly relies on the selection and design of cell geometry topologies, such as reentrant structures [20], honeycombs [21], beams [22,23], origami [24,25], and network unit cells [26,27]. Recently, the kirigami principle has gained prominence as a strategy that offers nonlinear large deformations for tailoring multiple mechanical properties [28–30]. More importantly, integrating bistability into the kinematics of kirigami designs enhances their appeal, allowing for self-locking and reversible transformations between stable configurations [31,32]. Such fascinating properties lead to kirigami applications in medical implants [33], shape morphing [34–36], wave controlling [37–39], and soft actuators and robotics [40,41].

Despite these advancements, the use of multistable kirigami in metamaterial inverse design remains limited, primarily due to the inability to parametric program a sufficient range of mechanical properties in conventional topology designs. On the one hand, the demands of

*Contact author: liboxjtu@xjtu.edu.cn
†Contact author: sunwenjie2017@xaut.edu

programming necessitate the tuning of richer mechanical properties with fewer parameters, thereby broadening the design space and making it amenable to algorithmic implementation. For instance, the aforementioned bistable auxetic cell has a limited isotropic expansion range, with a constant Poisson's ratio that restricts the variety of achievable shapes in the target. Symmetric geometries also result in isotropic stiffness, posing challenges for applications requiring varied load-bearing capacities in different directions. On the other hand, kirigami metamaterials are expected to evolve from bistable to multistable configurations since bistability offers only two stable states, which restricts their transformative capabilities. Relevant studies have characterized this phenomenon as a kind of phase transition with propagation through a multistable network, transforming cells from an open to a closed state as the domain wall passes by [42]. Consequently, additional frameworks for kirigami metamaterials are highly expected, given their potential.

To address the limitations of existing works, we introduce an "iD kirigami," an innovative inverse design platform based on a unified topology [43,44] that leverages kirigami geometry for programming and transforming mechanical behavior. By applying the principles of mechanism design, the geometry of such a kirigami pattern enables the achievement of anisotropic nonlinear mechanical responses, such as deformation and stiffness, which are governed by a limited set of parameters. This study first characterizes how these geometric parameters influence the desired properties. Subsequently, an inverse design process is implemented using a machine learning approach integrated with a genetic algorithm (ML-GA). To validate the programmable and transformable capabilities, we select target axisymmetric profiles for shape morphing, incorporating multistability to enhance functional reconfigurations. Overall, our platform offers a novel approach to designing multistable kirigami metamaterials, thereby paving the way for the development of smart structures.

II. ARCHITECTURE OF iD KIRIGAMI

Figure 1 presents an overview of the proposed iD kirigami framework. The basic kirigami is based on a unified cut topology featuring two cuts arranged on opposite sides. This design facilitates the generation of a family of parameterized kirigami cells through tessellation. When subjected to stretching, the kirigami geometry exhibits unique mechanical behaviors, particularly in terms of deformation and stiffness characteristics. By adjusting a minimal number of geometric parameters, these kirigami

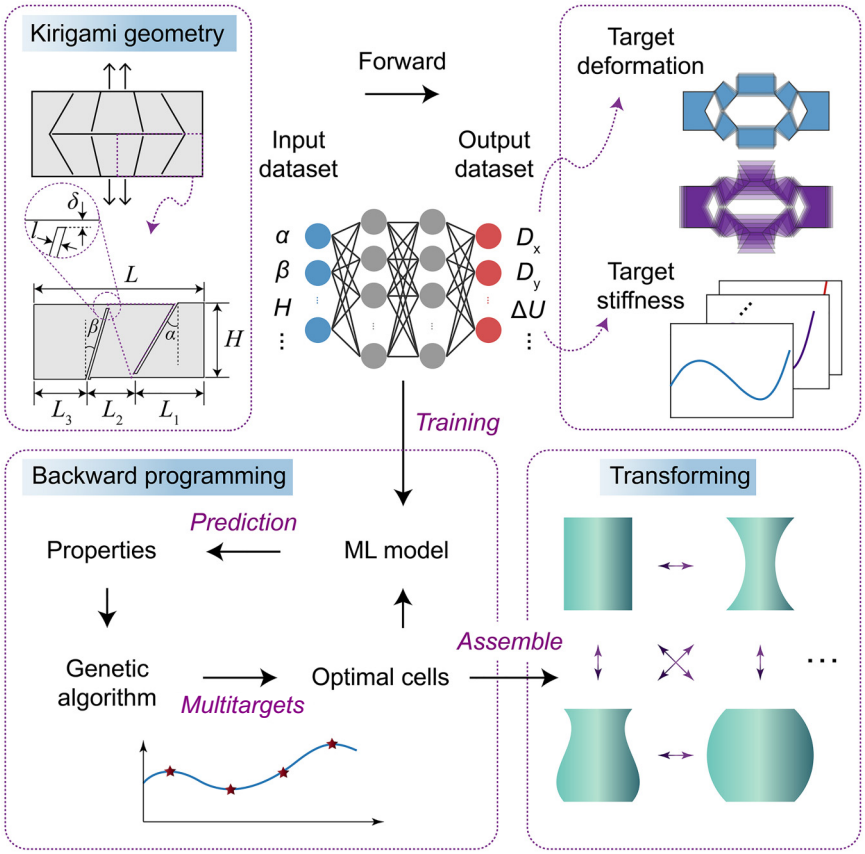

FIG. 1. Framework of the geometry-enabled shape programming and transforming utilizing multistable kirigami architectures.

cells can demonstrate alternating negative or positive Poisson's ratios. Furthermore, the intrinsic nonlinear stiffness of these cells enables programmable bistability. The synthesized mechanism inherent in the kirigami geometry allows for the independent design of mechanical characteristics, such as anisotropic deformation and energy barriers.

The rich mechanical responses are governed by geometry only, which satisfies the unified topology exactly. Therefore, a critical issue is characterizing how geometric parameters influence deformation and stiffness properties. Generally, the highly nonlinear mechanical behavior complicates the derivation of analytical solutions. Additionally, nonlinearity arising from soft materials and simplified geometric assumptions can introduce errors. Fortunately, parametric modeling of the kirigami cells via a finite element (FE) analysis is efficient and beneficial for inverse design applications. During the forward design stage, a library of bistable cells is constructed, offering a maximal design space of deformation and a sufficient tunability of energy barrier between the two stable states.

An inverse design workflow, illustrated in Fig. 1, combines a fully connected neural-network-based machine learning (ML) model with a genetic algorithm (GA). The ML model is trained using a dataset comprising two components: cell designs (input dataset) and mechanical responses (output dataset). Specifically, the FE model of the cells is built by parametric modeling via a PYTHON script. The mechanical responses of cells with different parameters are obtained from the FE simulations using ABAQUS/STANDARD 2017. The material of the kirigami cells is thermoplastic polyurethane (TPU). To characterize the mechanical response of the TPU material, a nearly incompressible two-parameter Mooney-Rivlin hyperelastic model is used, while $C_{10} = -11.60$ and $C_{01} = 20.79$ are adopted to model cells within all the FE simulations. The technical details are summarized in the Appendixes. For the application of anisotropic bistable cells in fields such as shape morphing, it is essential to consider both their deformation characteristics and energy barrier properties. The deformation of the kirigami cell must be carefully programmed to achieve the desired target shape, while the energy barrier plays a crucial role in providing sufficient stiffness to maintain stability in the final configuration. In this study, the concerned mechanical responses of cells with varying parameters are obtained from FE simulations via a PYTHON script. The ML model is then integrated with the GA as ML-GA to solve the inverse problem of identifying the optimal design based on target properties. The fast and accurate ML model enables the GA to explore

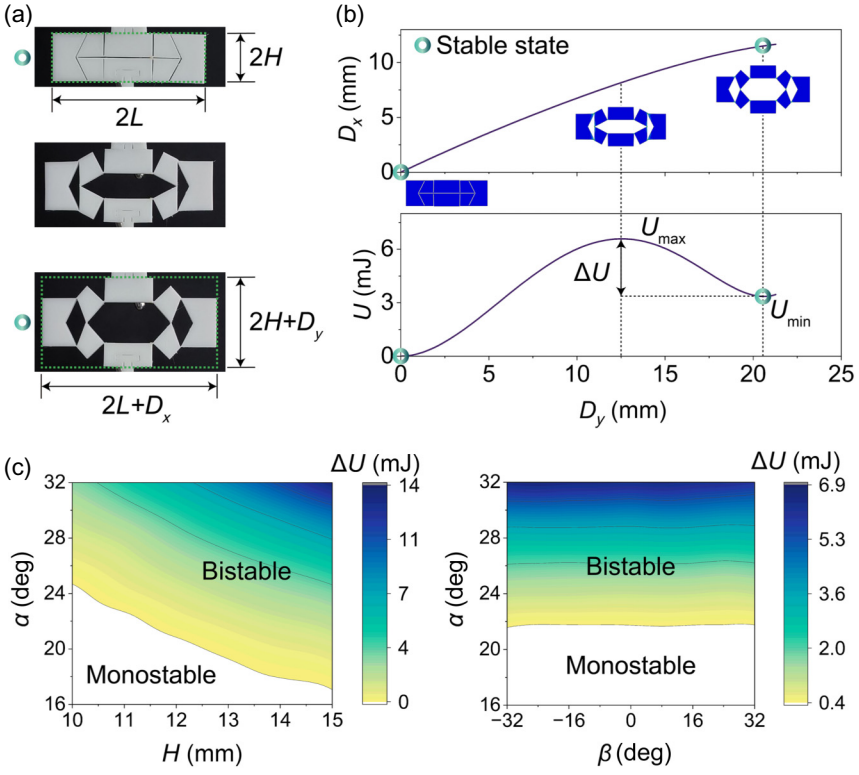

FIG. 2. Deformation and stiffness characteristics of a kirigami cell. (a) Configurations of the kirigami cell with defined displacements. (b) Anisotropic deformation and energy responses of the kirigami cell. (c) Parameters sweep and the selected bistable design space.

a vast design space that would be infeasible to investigate using FE simulations alone. The backward programming addresses multiple objectives, including target shape and stiffness. Subsequently, the selected optimal cells are strategically assembled to construct a 3D metastructure, such as a free-form surface or shell.

Once fabricated through 3D printing or assembly, the model can be actuated by stretching all cells toward their second stable state, resulting in a globally stable deployed surface. In this process, the anisotropic displacements of the cells dictate the inhomogeneous expansion, which is meticulously designed to morph the assembled structure into a target shape. To date, such mechanical metamaterials, once fabricated, possess only two stable configurations in conventional designs, with all the cells either open or closed. However, in our iD kirigami architecture, the geometric design permits cells to exist in different stable states even when connected without compromising overall stability. In other words, the transition between stable states does not propagate continuously among cells. Consequently, the ability to transform among several stable states significantly enriches the functional reconfiguration of the structure.

III. GEOMETRY-ENABLED DESIGN SPACE

A previous mechanism analysis [44] suggests that a kirigami design is well-suited for data-driven applications due to its ability to control a wide range of mechanical characteristics with only a few geometric parameters. The design space is constructed by using three primary parameters: H, α, and β. Unlike isotropic expansion, it is crucial to consider displacements in both the x- and y-direction, denoted as D_x and D_y, as illustrated in Fig. 2(a). Furthermore, the energy barrier, defined as $\Delta U = U_{\max} - U_{\min}$, represents the difference between the energies at local maximum and minimum points, as shown in Fig. 2(b). For a transition between two stable states, this energy barrier ΔU must be overcome; thus, it should be sufficiently large to ensure the stability of the kirigami cells.

To elucidate the relationship between bistability and geometry, we conducted a comprehensive parameter sweep on variables H and α. By simulating each sampled cell design, we evaluated the energy barriers, the results of which are summarized in Fig. 2(c). It is evident that an increase in either H or α leads to a corresponding increase in ΔU. When ΔU exceeds zero, strain energy barriers are formed, resulting in bistable states. Additionally, we performed a detailed parameter sweep on α and β while maintaining a constant value for H. Despite significant variations in β, the energy barriers of the cells remained largely unchanged, being predominantly influenced by α. In our subsequent analysis, we focus exclusively on bistable cells to construct our design space and further explore the relevant mechanical properties.

The correlation among the measured properties is illustrated in Fig. 3. Each data point represents the properties of a single parameterized kirigami pattern. The axes of the plot correspond to displacements in the x- and y-direction, while the energy barrier is indicated by the color of the data points. As depicted in Fig. 3, D_x exhibits a weak correlation with D_y, as a specific D_x can result in various D_y values. This wide range of anisotropic deformation in both directions is sufficient for programming multiple target shapes. Furthermore, the energy barrier ΔU shows a correlation with displacements D_x and D_y, as evidenced by the

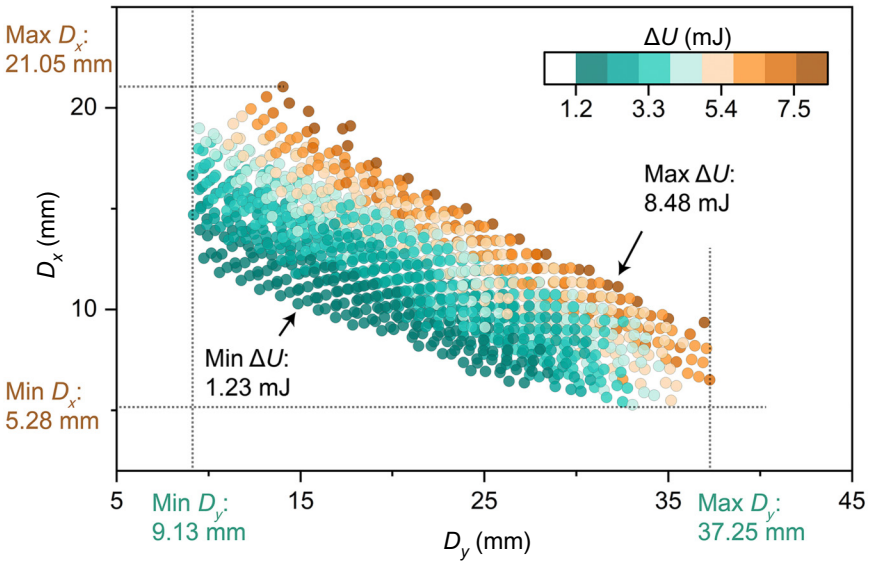

FIG. 3. Visualization and correlations of the mechanical properties in the selected design space.

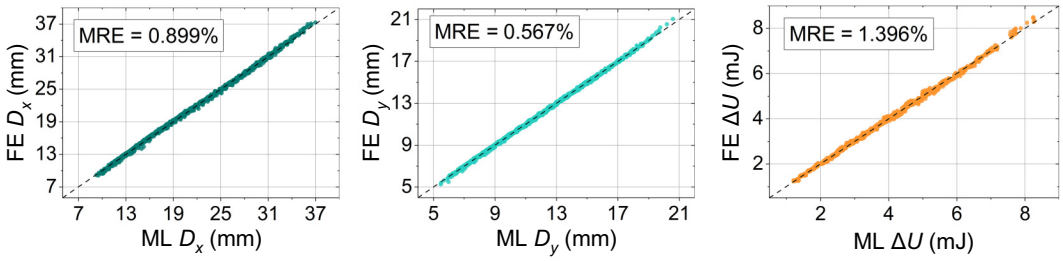

FIG. 4. Comparison of the FE mechanical properties and the ML predicted properties.

color distribution in the plot. The properties of the kirigami cells cover a range of mechanical properties with minimal gaps, which is crucial for training a machine learning model.

The kirigami geometry can be effectively parameterized using only three variables, making it highly suitable for ML modeling. The parameters H, α, and β serve as input data to construct a dataset for ML training. The FE models of the kirigami cells are developed, and their mechanical characteristics, namely D_x, D_y and ΔU, are obtained through simulation as output data. Subsequently, an ML model is constructed using the open-source neural-network library PyTorch, see Appendix D. This ML model was finally integrated with a GA to address the inverse problem of identifying the optimal design that satisfies multiobjectives.

This study employs two methods, i.e., FE simulation and the trained ML model, to predict the mechanical properties of kirigami patterns. A comparison of the mechanical properties calculated via the FE simulation and those predicted by the trained ML model is made. The results from the testing set are depicted in Fig. 4, where the data points scatter around the straight-line $y = x$, indicating that the ML model does not suffer from overfitting and is applicable for prediction and optimization across the entire design space. Additionally, Fig. 4 presents the mean relative error (MRE) for each design parameter, confirming the high prediction accuracy of the ML model.

IV. PROGRAMMABLE SHAPE MORPHING

We then focus on the design of kirigami structures that mimic target axisymmetric profiles, such as the jar shape shown in Fig. 5. To simplify the design, all the selected rectangular kirigami cells have the same initial width of $2L$ and height of $2H$. The initial closed state is defined as a stable state "0". On connecting nonrotating tiles, various cells can be conveniently linked to form a sheet. This

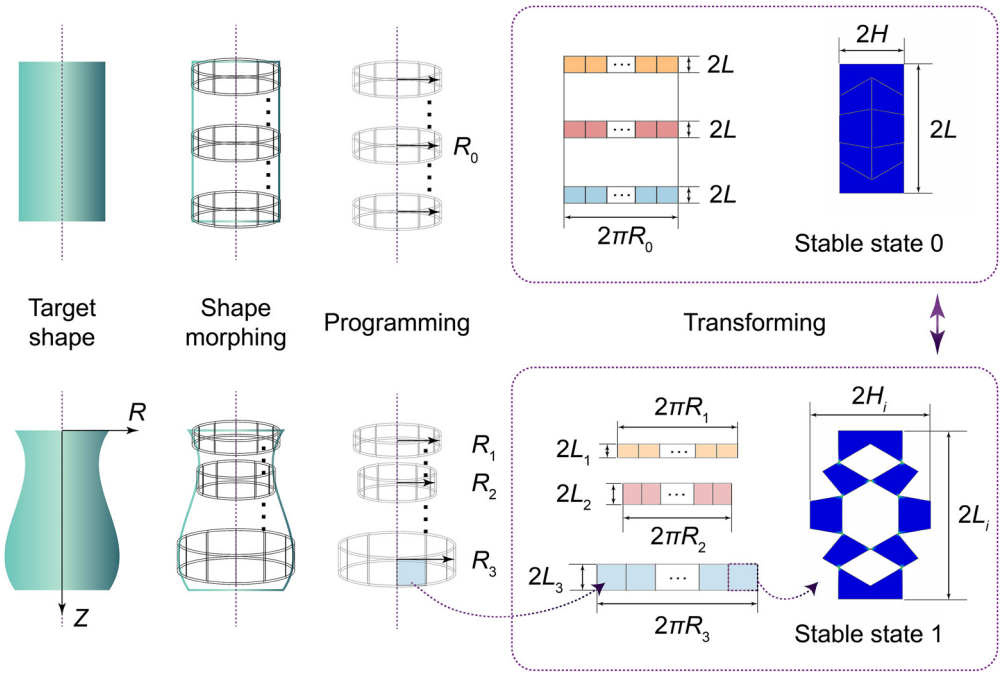

FIG. 5. Target axisymmetric profile shape, programming, and transforming process.

sheet can then be rolled into a cylindrical shell by connecting its ends, transforming the initial rectangular kirigami sheet into a cylinder with all the cells in a stable state "0". Figure 5 inversely illustrates how a cylinder is composed of kirigami cells.

Uniquely, we populate the cylinder with bistable cells that offer programmable anisotropic deformation at their second stable states (i.e., stable states "1"). By setting the cut angles α and β of each kirigami cell, the entire cylindrical shell can be expanded and morphed into a revolving shell with a target axisymmetric profile. Due to the energy barrier, the resulting shell is globally stable and requires no external forces to maintain its shape, allowing it to reversibly transform between the two stable states. To morph a kirigami shell into a target shape, such as the jar, the target profile is segmented according to the size of the kirigami cells. Each row can be rolled into a segment of the whole shell and, for such an axisymmetric shell, all the kirigami cells in each row are identical. Figure 5 reports the relationship between the local radius of the revolving shell and the size of the opened cells in the corresponding row. The number of segments n for all the rows is the same, and it satisfies the following condition:

$$2\pi R_i = n(2H + D_{yi}), \tag{1}$$

where R_i is the radius of the ith row and D_{yi} is the y-displacement of the cells in it. The length of the ith segment Z_i is calculated as

$$Z_i = 2L + D_{xi}. \tag{2}$$

Following the geometric relationship, we employ the ML-GA to identify the optimal cells for each segment sequentially. As illustrated in Fig. 6(a), the coordinates of the ith segment are denoted by (Z_i, R_i). We define a function, get_dis(Z_i, R_i), to calculate the distance between the point and the target profile. The evaluation function of the GA is subsequently formulated as follows:

$$\begin{cases} f_1 = \min(\text{get\_dis}(Z_i, R_i)) \\ f_2 = \max(\Delta U) \end{cases}. \tag{3}$$

This problem inherently involves multiple objectives: the optimal cells must not only result in the closest point on the target profile but also possess a sufficiently large energy barrier to ensure the stability of the entire structure.

Figure 6(b) demonstrates an example where the target shape is derived by sampling the target points (indicated by star symbols) on the profile. Polynomial fitting is employed to approximate and plot the curve representing the target shape, with the orange line indicating the fitting profile. By executing the ML-GA for each segment, we obtain the inverse design result of this profile. The comparison in Fig. 6(b) reveals that slight off-target deviations occur only at positions where the curvature changes rapidly, yet the overall result is excellent.

V. MULTISTABLE CONFIGURATION TRANSFORMING

The performance of the proposed framework is demonstrated through a simple forearm shape example. As illustrated in Fig. 7(a), three distinct rows of kirigami cells, each corresponding to a unique set of geometric parameters, are fabricated with notches to facilitate connection. To effectively encode the anisotropic deformation within the initial cylindrical shell, optimal geometric parameters are determined using the ML-GA inverse design process. This process addresses the multiobjective problem, as expressed in Eq. (3), by considering stiffness to enhance the stability of the deformed structure. Notably, each row consists of identical kirigami cells of the same initial size, allowing them to form a flat kirigami sheet when connected. This

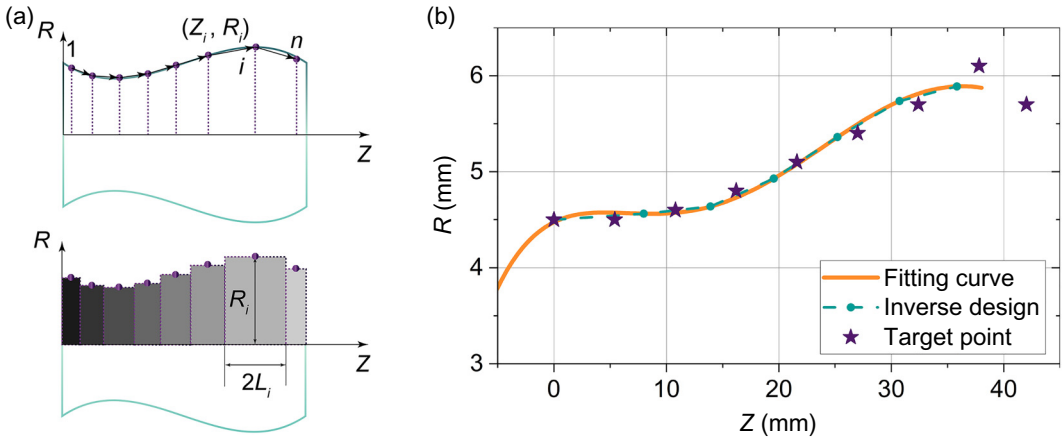

FIG. 6. Inverse design of the jar axisymmetric profile. (a) Schematic of the design process. (b) Comparison of the design results and the target profile.

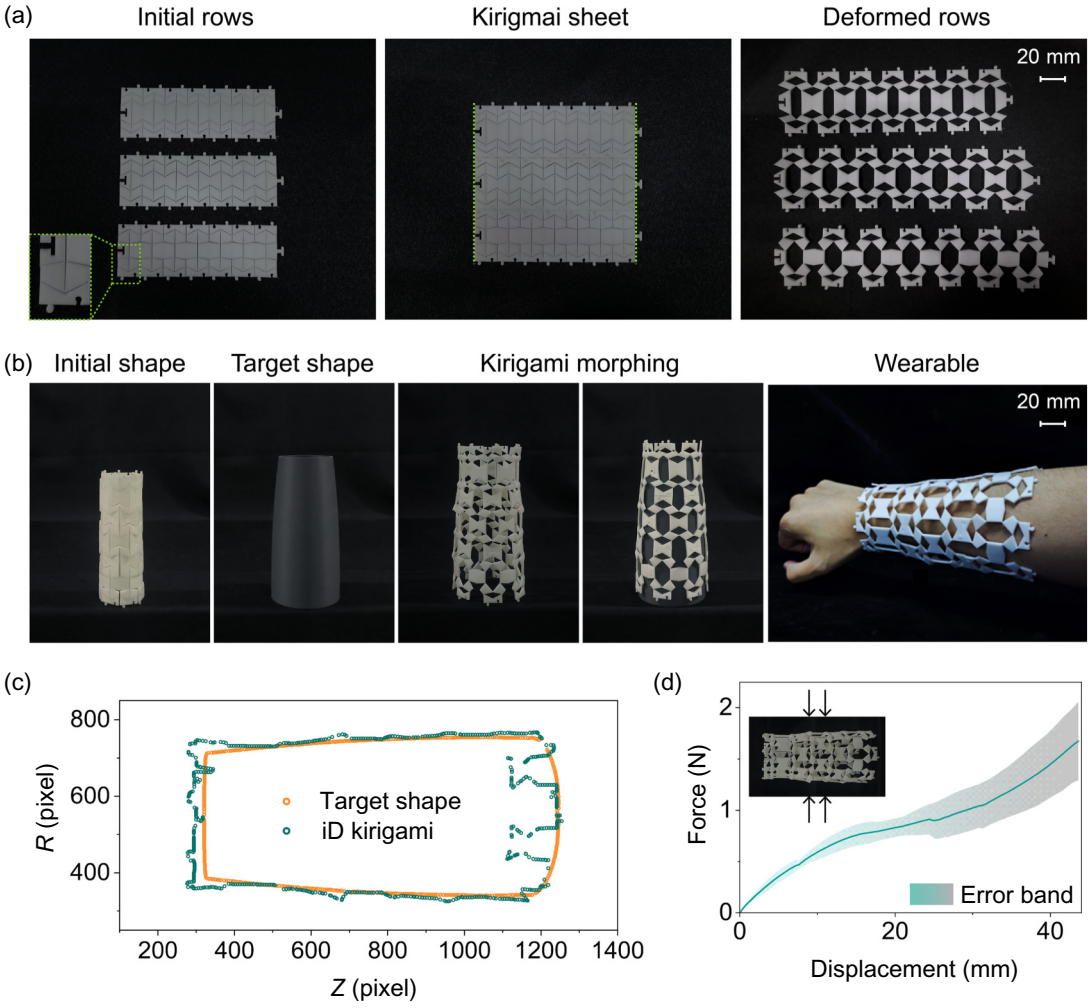

FIG. 7. iD kirigami adapted to the specific geometry of the forearm. (a) Configurations of the optimal kirigami rows and sheet. (b) Kirigami morphed into a wearable forearm shape. (c) Comparison of the iD kirigami and the target shape. (d) Force-displacement response during loading.

sheet is subsequently rolled into a cylindrical shell by joining its edges, as indicated by the dotted lines in Fig. 7(a). For comparison, the deformed configurations of the three rows are also presented, revealing a significant difference in length among them.

The sheet constructed by assembling three rows of kirigami cells is then rolled into a complete shell. Upon stretching, the iD kirigami structure expands and morphs into the desired target shape, as shown in Fig. 7(b). Given that the target is a specific forearm shape, we further illustrate the promising application of the kirigami shell as a wearable device. In Fig. 7(c), the axisymmetric profiles of both the target model and the deformed kirigami structure are extracted from images, allowing for a quantitative comparison via pixels. The deformed iD kirigami closely aligns with the target shape, demonstrating a high degree of accuracy. However, discrepancies arise in areas where the curvature changes rapidly, primarily due to the local out-of-plane deformation of the tiles. To address this issue, it is anticipated that scaling the cells and increasing the tessellation density of the rows will result in a "smoother" configuration for the entire structure, thereby minimizing these errors. Furthermore, the force-displacement response is explicitly measured to verify the stiffness, as depicted in Fig. 7(d). During compression, the kirigami structure undergoes significant deformation; however, once the load is removed, the structure returns to its open stable state with a minimal state switching of the cells observed.

The transformable capabilities enabled by multistability in kirigami architectures are demonstrated in this study. Our geometric design enables the upper and lower parts of the cells in each row to be opened or closed independently, as illustrated in Fig. 8(a). The kirigami cylinder, in this instance, comprises two rolled rows, and four binary numbers are employed to represent the multistable configurations. Figure 8(b) shows snapshots of the kirigami

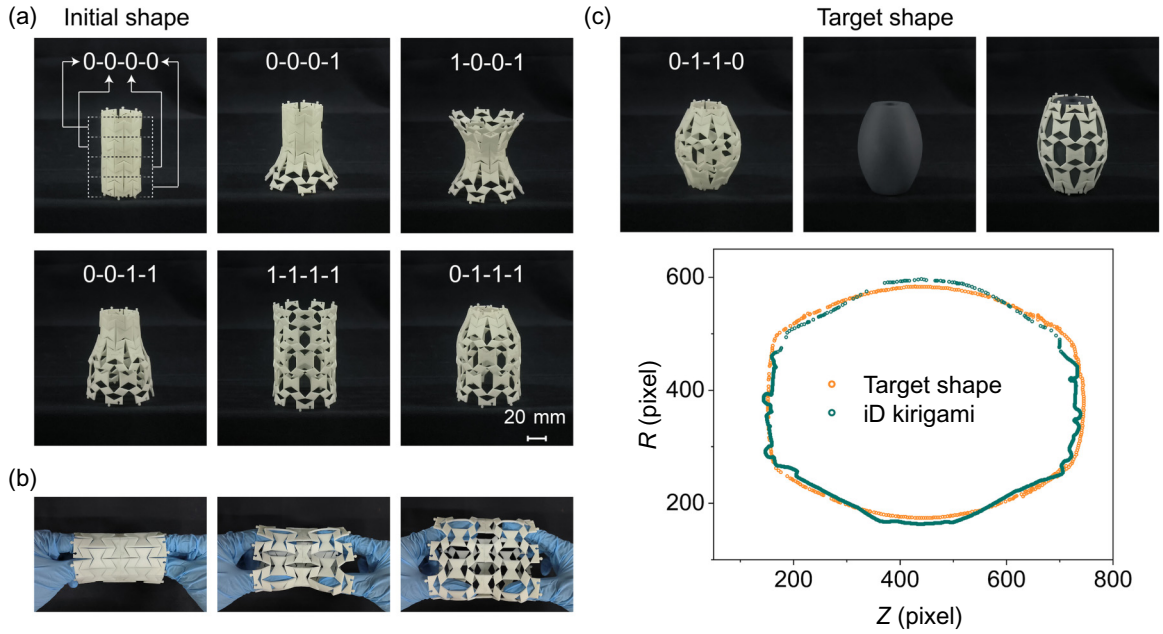

FIG. 8. Configuration transforming of the multistable kirigami. (a) Multistable configurations of the kirigami cylindrical shell represented with binary numbers. (b) Snapshots of the deployment of the kirigami shell by hand. (c) The "0-1-1-0" configuration morphed into an olive shape.

cylindrical shell deploying from the "0-0-0-0" to the "1-1-1-1" configuration under internal expansion tension. These four numbers can be arranged in various ways, but not all the kirigami structures that result exhibit sufficient stability. In Fig. 8, we present only the configurations that possess adequate stiffness. Our kirigami architecture, represented by different binary numbers, displays a wide range of configurations and the ability to transform between them. Notably, the "0-1-1-0" configuration is programmed to form an olive shape, as depicted in Fig. 8(c). The correlation of pixels indicates that the contour of the "0-1-1-0" configuration closely matches the target shape.

VI. CONCLUSION

In summary, a framework utilizing kirigami geometry for programming and transforming mechanical characteristics is proposed. This framework involves training a machine learning model using geometric parameters as input data and mechanical responses as output data. By integrating this model with a genetic algorithm, an inverse design process is achieved that satisfies multiple objectives, including desired deformation and maximum stiffness. Optimal kirigami cells are then rationally assembled and globally morphed into the target shape upon stretching. The significance of geometry in expanding the design space and simplifying the algorithm workflow is demonstrated through specific examples. This framework also serves as a tool aimed at accelerating progress in tailoring mechanical characteristics. The proposed multistable kirigami structures switch easily between different configurations through mechanical actuation only, which has great application potential in transforming robots, multifrequency wave controlling, and so on.

ACKNOWLEDGMENTS

The authors gratefully acknowledge the financial support provided by the National Natural Science Foundation of China (Grant No. 52475030) and the Natural Science Foundation of Shaanxi Province (Grant No. 2024JC-YBQN-0028).

DATA AVAILABILITY

No data were created or analyzed in this study.

APPENDIX A: FABRICATION AND MECHANICAL TESTING

All the specimens were fabricated using Raise3D E2 (Raise3D, China) via fused deposition modeling additive manufacturing technology. White thermoplastic polyurethane (TPU 95A) has been used as the constitute material for fabricating the specimens.

The nominal stress-nominal strain curve of the TPU material has been obtained by performing uniaxial tensile tests on dumbbell-shaped specimens using a testing machine (ZHIQU ZQ-990B, China) with a 100-N load cell. As shown in Fig. 9, the TPU material exhibits approximate hyperelastic properties and it is found to be

effectively captured using a nearly incompressible two-parameter-featured Mooney-Rivlin hyperelastic model.

To be specific, the Mooney-Rivlin hyperelastic model used here is given by

$$W = C_{10}(I_1 - 3) + C_{01}(I_2 - 3), \tag{A1}$$

where W is the strain energy density, and I_1 and I_2 are the first and second invariants of the left Cauchy-Green tensor of the deformation gradient, respectively. For the uniaxial tension, the corresponding stress can be written as

$$\sigma = 2C_{10}(\lambda - \lambda^{-2}) + 2C_{10}(1 - \lambda^{-3}), \tag{A2}$$

where σ is the uniaxial tensile stress and λ is the percentage elongation in the loading direction. By fitting the above equation against the experimental results, the material constants can be obtained as $C_{10} = -11.60$ and $C_{01} = 20.79$.

APPENDIX B: GEOMETRIC MODEL

In this research, we define all the single kirigami cells in 2D and keep the thickness sufficiently large to reduce out-of-plane buckling during stretching. Specifically, a thickness $t = 2$ mm is adopted for all the kirigami cells. All the in-plane geometric parameters of the cells are defined according to the labels shown in Fig. 9.

In our input data, including a building block width $L = 40$ mm, L_1 can be calculated as follows: $L_1 = H\tan\alpha + 12$. In addition, the value of L_2 for all the cells is set at 9 mm and values of L_3 are then given as $L_3 = L - L_1 - L_2$. To enhance the bistable behavior, δ and l should be as small as possible while still ensuring robustness under cyclic loading. Empirically, we chose $\delta = 0.5$ mm and $l = 0.6$ mm, which are easy to fabricate. Notably, geometric dimensions can be scaled according to the specific targets of the shape morphing as long as they maintain the topology.

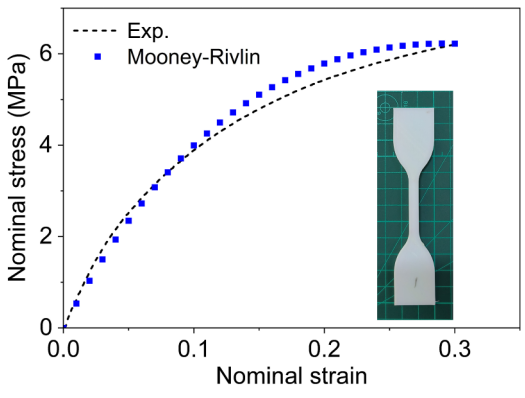

FIG. 9. Comparison between experimental and Mooney-Rivlin fit for the nominal stress-nominal strain curve of the TPU material used to model unit cells within the FE simulations.

APPENDIX C: FE SIMULATIONS

All the simulations are carried out in ABAQUS/STANDARD 2017 and the models are discretized with quadratic plane stress elements (CPS4R and CPS3). In the simulations, local fine meshes are applied to all the hinge areas since these regions are highly deformed with severe stress concentration and mesh sensitivity is conducted to ensure numerical convergence. The material behavior of the kirigami cells is captured using a Mooney-Rivlin hyperelastic model with parameters C_{10} and C_{01} of the fitted model in Fig. 9.

We model the structure in the displacement-control quasistatic case, and the deformation can be captured by dynamic and implicit algorithms. To be specific, as for the loading process, displacement-control loading is applied to the structure, leading to a snap-through of the bistable cells. The unloading is realized by removing the loading. Here, the displacement is prescribed and the force is extracted as a reaction from simulation. We consider a large deformation of the structures and the geometric nonlinearities are taken into account. A simplified contact law is assigned to the model with a hard contact for normal behavior and a frictionless tangential behavior. As mentioned in the main text, we fully constrain the middle section of the lower edge while vertical prescribed displacement is applied to the middle section of its upper edge. In our study, all the FE models are built using parametric modeling via a PYTHON script. After running the simulations, the PYTHON script is used to extract the concerned mechanical responses from the FE result files, which are then used in the ML training.

APPENDIX D: ML MODEL

In this study, the ML model is designed with an input layer of dimensions 5×1, a hidden layer of dimensions 12×1, and an output layer of dimensions 8×1. Various configurations for the hidden layers and their sizes were explored to optimize the model's performance. The mean relative error (MRE) was employed as the loss function to evaluate the model. Following this, a proper optimizer, which is used to shape and mold the model to a more accurate form during the training process, needs to be determined. A stochastic gradient descent optimizer and an Adam optimizer are used in this work. In the end, we examined several activation functions for the hidden layers and output layers, including the rectified linear unit (ReLu) activation function, sigmoid activation function, and linear activation function. At this point, a set of models can be constructed due to multiple combinations. In the training process, we examine these models and determine one model that yields the most satisfactory result. Besides, we find the ideal values of the weight matrixes for all the layers that minimize the loss function. The weight matrixes are used to define the relationship between each layer in the

ML model. Consequently, a well-trained ML model was developed to accurately represent the relationship between geometric parameters and mechanical properties within the training set. This ML model was subsequently integrated with a GA (ML-GA) to address the inverse problem of identifying the optimal design that satisfies multiobjectives. Specifically, the mean relative error is calculated via

$$\mathrm{MRE} = \frac{1}{n}\sum_{i=1}^{n}\left|\frac{y_i - \hat{y}_i}{y_i}\right|, \tag{D1}$$

where y_i is the mechanical properties obtained from the FE simulations and $\bar{y}$ is the corresponding average of them; $\hat{y}_i$ is the mechanical properties from the ML predictions.

[1] E. Tezsezen, D. Yigci, A. Ahmadpour, and S. Tasoglu, AI-Based Metamaterial Design, ACS Appl. Mater. Interfaces **16**, 29547 (2024).

[2] X. H. Sun, K. Zhou, F. Demoly, R. R. Zhao, and H. J. Qi, Perspective: Machine Learning in Design for 3D/4D Printing, J. Appl. Mech. **91**, 030801 (2024).

[3] C. P. Ma, Y. L. Chang, S. Wu, and R. R. Zhao, Deep Learning-Accelerated Designs of Tunable Magneto-Mechanical Metamaterials, ACS Appl. Mater. Interfaces **14**, 33892 (2022).

[4] X. Y. Zheng, X. B. Zhang, T. T. Chen, and I. Watanabe, Deep Learning in Mechanical Metamaterials: From Prediction and Generation to Inverse Design, Adv. Mater. **35**, 2302530 (2023).

[5] P. Sinha and T. Mukhopadhyay, Programmable multi-physical mechanics of mechanical metamaterials, Mater. Sci. Eng., R **155**, 100745 (2023).

[6] R. van Mastrigt, M. Dijkstra, M. van Hecke, and C. Coulais, Machine Learning of Implicit Combinatorial Rules in Mechanical Metamaterials, Phys. Rev. Lett. **129**, 198003 (2022).

[7] Z. Chai, Z. Zong, H. Yong, X. Ke, J. Zhu, H. Ding, C. F. Guo, and Z. Wu, Tailoring Stress–Strain Curves of Flexible Snapping Mechanical Metamaterial for On-Demand Mechanical Responses via Data-Driven Inverse Design, Adv. Mater. **36**, 2404369 (2024).

[8] X. Sun, L. Yue, L. Yu, H. Shao, X. Peng, K. Zhou, F. Demoly, R. Zhao, and H. J. Qi, Machine Learning-Evolutionary Algorithm Enabled Design for 4D-Printed Active Composite Structures, Adv. Funct. Mater. **32**, 2109805 (2021).

[9] X. C. Ni, H. W. Luan, J. T. Kim, S. Rogge, Y. Bai, J. W. Kwak, S. L. Liu, D. S. Yang, S. Li, S. P. Li, *et al.*, Soft shape-programmable surfaces by fast electromagnetic actuation of liquid metal networks, Nat. Commun. **13**, 5576 (2022).

[10] D. M. J. Dykstra and C. Coulais, Inverse design of multi-shape metamaterials, Phys. Rev. Appl. **22**, 064013 (2024).

[11] C. L. Zhu, E. A. Bamidele, X. Y. Shen, G. M. Zhu, and B. W. Li, Machine Learning Aided Design and Optimization of Thermal Metamaterials, Chem. Rev. **124**, 4258 (2024).

[12] Y. Y. Lu, D. P. Kong, G. Yang, R. H. Wang, G. Y. Pang, H. Y. Luo, H. Y. Yang, and K. C. Xu, Machine Learning-Enabled Tactile Sensor Design for Dynamic Touch Decoding, Adv. Sci. **10**, 2303949 (2023).

[13] Y. J. Wang, M. L. Adam, Y. L. Zhao, W. H. Zheng, L. B. Gao, Z. Y. Yin, and H. T. Zhao, Machine Learning-Enhanced Flexible Mechanical Sensing, Nano-Micro Lett. **15**, 55 (2023).

[14] Z. G. Liu, M. K. Cai, S. D. Hong, J. L. Shi, S. Xie, C. Liu, H. F. Du, J. D. Morin, G. Li, L. Wang, *et al.*, Data-driven inverse design of flexible pressure sensors, Proc. Natl. Acad. Sci. U. S. A. **121**, 232022212 (2024).

[15] Y. Bai, H. L. Wang, Y. G. Xue, Y. X. Pan, J. T. Kim, X. C. Ni, T. L. Liu, Y. Y. Yang, M. D. Han, Y. G. Huang, *et al.*, A dynamically reprogrammable surface with self-evolving shape morphing, Nature **609**, 701 (2022).

[16] X. Cheng, Z. C. Fan, S. L. Yao, T. Q. Jin, Z. Y. Lv, Y. Lan, R. H. Bo, Y. T. Chen, F. Zhang, Z. M. Shen, *et al.*, Programming 3D curved mesosurfaces using microlattice designs, Science **379**, 1225 (2023).

[17] Q. Zeng, S. Duan, Z. Zhao, P. Wang, and H. Lei, Inverse Design of Energy-Absorbing Metamaterials by Topology Optimization, Adv. Sci. **10**, 2204977 (2022).

[18] Z. F. Wu, B. L. Zhu, R. X. Wang, and X. M. Zhang, Design of mechanical metamaterial for energy absorption using a beam with a variable cross-section, Mech. Mach. Theory **176**, 105027 (2022).

[19] B. L. Deng, A. Zareei, X. X. Ding, J. C. Weaver, C. H. Rycroft, and K. Bertoldi, Inverse Design of Mechanical Metamaterials with Target Nonlinear Response via a Neural Accelerated Evolution Strategy, Adv. Mater. **34**, 2206238 (2022).

[20] H. Pahlavani, M. Amani, M. C. Saldívar, J. Zhou, M. J. Mirzaali, and A. A. Zadpoor, Deep learning for the rare-event rational design of 3D printed multi-material mechanical metamaterials, Commun. Mater. **3**, 46 (2022).

[21] Y. Li, S. Coros, and B. Thomaszewski, Neural Metamaterial Networks for Nonlinear Material Design, ACM Trans. Graphics **42**, 1 (2023).

[22] K. Liang, Y. G. Wang, Y. J. Luo, A. Takezawa, X. P. Zhang, and Z. Kang, Programmable and multistable metamaterials made of precisely tailored bistable cells, Mater. Des. **227**, 111810 (2023).

[23] F. Liu, X. H. Jiang, X. T. Wang, and L. F. Wang, Machine learning-based design and optimization of curved beams for multistable structures and metamaterials, Extreme Mech. Lett. **41**, 101002 (2020).

[24] Y. Deng, W. X. Liu, Y. K. Cheung, Y. K. Li, W. Hong, and H. Y. Yu, Curved display based on programming origami tessellations, Microsyst. Nanoeng. **7**, 101 (2021).

[25] K. Xiao, Z. H. Liang, B. H. Zou, X. Zhou, and J. H. Ju, Inverse design of 3D reconfigurable curvilinear modular origami structures using geometric and topological reconstructions, Nat. Commun. **13**, 7474 (2022).

[26] H. Pahlavani, K. Tsifoutis-Kazolis, M. C. Saldivar, P. Mody, J. Zhou, M. J. Mirzaali, and A. A. Zadpoor, Deep Learning for Size-Agnostic Inverse Design of Random-Network 3D Printed Mechanical Metamaterials, Adv. Mater. **36**, 2303481 (2023).

[27] T. Q. Jin, X. Cheng, S. W. Xu, Y. C. Lai, and Y. H. Zhang, Deep learning aided inverse design of the buckling-guided

assembly for 3D frame structures, J. Mech. Phys. Solids **179**, 105398 (2023).
[28] L. Jin and S. Yang, Engineering Kirigami Frameworks Toward Real-World Applications, Adv. Mater. **36**, 2308560 (2023).
[29] G. P. T. Choi, L. H. Dudte, and L. Mahadevan, Programming shape using kirigami tessellations, Nat. Mater. **18**, 999 (2019).
[30] P. Celli, C. McMahan, B. Ramirez, A. Bauhofer, C. Naify, D. Hofmann, B. Audoly, and C. Daraio, Shape-morphing architected sheets with non-periodic cut patterns, Soft Matter **14**, 9744 (2018).
[31] C. G. Jiang, F. Rist, H. Wang, J. Wallner, and H. Pottmann, Shape-morphing mechanical metamaterials, Comput.-Aided Des. **143**, 103146 (2022).
[32] H. Cho and D. Kim, Controlling the stiffness of bistable kirigami surfaces via spatially varying hinges, Mater. Des. **231**, 112053 (2023).
[33] Y. J. Lee, S. K. Kanchwala, H. Cho, J. C. Jolly, E. Jablonka, M. Tanis, R. D. Kamien, and S. Yang, Natural Shaping of Acellular Dermal Matrices for Implant-Based Breast Reconstruction via Expansile Kirigami, Adv. Mater. **35**, 2208088 (2022).
[34] X. Ma, Z. Wang, and P. Yan, Bistable shell enabled reprogrammable shape-morphing kirigami metamaterials, Appl. Mater. Today **36**, 102031 (2024).
[35] X. Ying, D. Fernando, and M. A. Dias, Inverse design of programmable shape-morphing kirigami structures, Int. J. Mech. Sci. **286**, 109840 (2025).
[36] X. X. Dang, F. Feng, H. L. Duan, and J. X. Wang, Theorem on the Compatibility of Spherical Kirigami Tessellations, Phys. Rev. Lett. **128**, 035501 (2022).
[37] J. W. Pan, M. Meloni, S. D. Kim, Q. Zhang, and J. G. Cai, Aperture size control in kirigami metamaterials: Towards enhanced performance and applications, Extreme Mech. Lett. **73**, 102266 (2024).
[38] Y. L. Zheng, K. Chen, and Y. J. Feng, A Review of Kirigami/Origami Metasurfaces for Controlling Electromagnetic Waves, Ann. Phys. **536**, 2400213 (2024).
[39] H. Khosravi and S. Y. Li, Tunable Wave-Propagation Band gap via Stretching Kirigami Sheets, Phys. Rev. Appl. **17**, 064054 (2022).
[40] Y. Y. Hong, Y. D. Chi, S. Wu, Y. B. Li, Y. Zhu, and J. Yin, Boundary curvature guided programmable shape-morphing kirigami sheets, Nat. Commun. **13**, 530 (2022).
[41] J. Q. Wang, R. C. Wang, Z. X. Zhu, K. Zhou, and D. Wang, Untethered kirigami soft robots with programmable locomotion, Appl. Phys. Rev. **10**, 041405 (2023).
[42] L. Jin, R. Khajehtourian, J. Mueller, A. Rafsanjani, V. Tournat, K. Bertoldi, and D. M. Kochmann, Guided transition waves in multistable mechanical metamaterials, Proc. Natl. Acad. Sci. U. S. A. **117**, 2319 (2020).
[43] Y. Q. Yin, Y. Z. Hu, Y. P. Zhang, Y. Yu, R. Y. Bai, Y. J. Wang, B. Li, and G. M. Chen, Programmable multistable kirigami chain: Decoupling energy barrier and snapping force/displacement in a unified topology, Mech. Mach. Theory **199**, 105691 (2024).
[44] Y. Q. Yin, B. Li, Y. Z. Hu, Y. Yu, Y. P. Zhang, X. F. Liu, R. Y. Bai, and G. M. Chen, A unified cut topology that endows programmable bistability in modular kirigami morphing structures, Cell Rep. Phys. Sci. **5**, 102335 (2024).

Correction: The affiliation indicator for the last author was set incorrectly during the production process and has been fixed.